Available online at www.sciencedirect.com
ScienceDirect
Trans. Nonferrous Met. Soc. China 30(2020) 710−726
Transactions of Nonferrous Metals Society of China
www.tnmsc.cn

High temperature deformation behavior and microstructure evolution of wrought nickel-based superalloy GH4037 in solid and semi-solid states

Ju-fu JIANG[1], Guan-fei XIAO[1], Ying WANG[2], Ying-ze LIU[1], Ying ZHANG[1]

1. School of Materials Science and Engineering, Harbin Institute of Technology, Harbin 150001, China;
2. School of Mechatronics Engineering, Harbin Institute of Technology, Harbin 150001, China

Received 25 June 2019; accepted 6 December 2019

Abstract: Cylindrical samples of Ni-based GH4037 alloy were compressed at solid temperatures (1200, 1250 and 1300 °C) and semi-solid temperatures (1340, 1350, 1360, 1370 and 1380 °C) with different strain rates of 0.01, 0.1 and 1 s^{-1}. High temperature deformation behavior and microstructure evolution of GH4037 alloy were investigated. The results indicated that flow stress decreased rapidly at semi-solid temperatures compared to that at solid temperatures. Besides, the flow stress continued to increase after reaching the initial peak stress at semi-solid temperatures when the strain rate was 1 s^{-1}. With increasing the deformation temperature, the size of initial solid grains and recrystallized grains increased. At semi-solid temperatures, the grains were equiaxed, and liquid phase existed at the grain boundaries and inside the grains. Discontinuous dynamic recrystallization (DDRX) characterized by grain boundary bulging was the main nucleation mechanism for GH4037 alloy.

Key words: nickel-based superalloy; high temperature deformation; semi-solid; microstructure evolution; dynamic recrystallization

1 Introduction

Generally, metal materials experience complex deformation during hot forming process [1]. The deformation mechanisms include work hardening (WH), dynamic recovery (DRV) and dynamic recrystallization (DRX) [2,3]. High temperature deformation behaviors of the metal materials are significantly affected by deformation temperature, strain rate and flow stress [4−6]. In the meantime, the microstructures of deformed parts are closely related to deformation parameters, and the results of hot compression are critical to the correct numerical simulation and the reasonable optimization of hot forming process. Thus, it is necessary to investigate the effects of hot deformation parameters on deformation behaviors of alloys.

Semi-solid processing (SSP) is a potential near-net metal forming method to fabricate products in semi-solid state [7]. It has some advantages over traditional casting methods and forging methods because of the special forming temperature range [8]. Compared with traditional casting methods, the products fabricated by semi-solid processing have less defects such as segregation, porosity and shrinkage [9,10]. Compared with conventional forging methods, semi-solid processing can fabricate products with complex geometry because of higher deformation homogeneity and smaller deformation resistance of semi-solid billets [11]. The products fabricated by semi-solid forming method will undergo varying degrees of deformation to refine the microstructure and improve the mechanical properties. Therefore, it is necessary to carry out semi-solid compression

Foundation item: Project (51575127) supported by the National Natural Science Foundation of China
Corresponding author: Ju-fu JIANG, Tel: +86-18746013176, E-mail: jiangjufu@hit.edu.cn;
Ying WANG, Tel:+86-15945697615, E-mail: wangying1002@hit.edu.cn
DOI: 10.1016/S1003-6326(20)65248-7

tests to investigate the microstructure evolution and deformation mechanism. A lot of high temperature deformation experiments have been conducted on semi-solid state of aluminum alloys [12−14], magnesium alloys [15,16], titanium alloys [17,18] and steels [19,20]. The results indicated that these alloys exhibited lower deformation resistance and excellent flowing property in semi-solid state because of the existence of liquid phase in the semi-solid billets.

Ni-based superalloys are a kind of excellent metal materials with many outstanding properties such as high temperature strength, toughness, the resistance to oxidation and abrasion [21]. Due to these superior properties, Ni-based superalloys are widely used in many significant industrial fields including aircraft, gas turbine engines, turbine disks, turbine blades and many other high temperature applications [22−24]. The products of Ni-based superalloys are mainly fabricated by traditional casting and forging methods [25]. High temperature deformation of superalloys was mainly investigated in solid state. CHEN et al [26] investigated the DRX behavior of a typical nickel-based superalloy and proposed the segmented models to describe the kinetics of DRX by the hot compression tests. WU et al [27] studied the hot deformation behavior of Ni_3Al-based alloy and found that the DRX degree could be effectively enhanced with the increase of deformation temperature and the decrease of strain rate. HE et al [28] investigated the microstructure evolutions and nucleation mechanisms of DRX of a powder metallurgy Ni-based superalloy during hot compression. However, the studies of Ni-based superalloys on semi-solid deformation are limited and the nucleation mechanisms are unclear.

In this study, high temperature deformation of nickel-based superalloy GH4037 was implemented experimentally at solid temperatures and semi-solid temperatures, aiming at investigating the deformation behavior and microstructure evolution of superalloys in solid and semi-solid states. The effects of compression temperature, strain rate and flow stress on deformation behavior and microstructure evolution were investigated. The misorientation angle evolution and dynamic recrystallization mechanisms were discussed.

2 Experimental

The commercial wrought Ni-based superalloy GH4037 was fabricated with a hot rolling process followed by a solution and aging treatment. The chemical composition (wt.%) of Ni-based superalloy GH4037 bar was 14.943% Cr, 5.612% W, 3.174% Mo, 2.122% Ti, 1.866% Al, 0.220% V, 0.019% Co and balanced Ni. The differential scanning calorimeter (STA449F3) was used to determine the solidus and liquidus temperatures. Based on the heat flow versus temperature curve, the solidus and liquidus temperatures were obtained, which were 1309 and 1405 °C, respectively. By integrating the data of the differential scanning calorimetry (DSC), the liquid volume fraction versus temperature curve of GH4037 was plotted, as shown in Fig. 1.

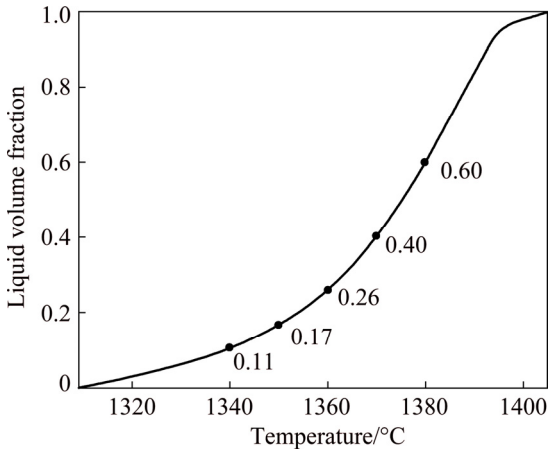

Fig. 1 Liquid volume fraction versus temperature curve of nickel-based superalloy GH4037

The compression specimens were cut into cylinders with a diameter of 8 mm and a length of 12 mm from the initial GH4037 alloy bar. The compression experiments were conducted by a Gleeble−1500D thermal-simulator. Temperatures of the compression specimens were measured by thermocouples to control the heat process and maintain the prescribed temperatures. Each compression specimen was heated to the required temperature with a heating rate of 10 K/s, and then soaked for 2 min to ensure the compression specimen in a thermal equilibrium state. Three solid deformation temperatures (1200, 1250 and 1300 °C) and five semi-solid deformation temperatures (1340, 1350, 1360, 1370 and 1380 °C) were applied at

three different strain rates (0.01, 0.1 and 1 s^{-1}), and the final height reduction was 70%. In order to freeze the microstructures at ambient temperatures, the compression specimens were quenched in cold water immediately after deformation. Then, the quenched deformation specimens were ground up to 2000 grit paper and polished with 1.5 μm diamond paste.

In order to investigate the influence of deformation parameters on microstructure evolution, optical microscope (OM) and electron backscatter diffraction (EBSD) technology were carried out. For OM observation, the metallographic specimens were etched with aqua regia solution of 50% HCl, 25% HNO_3, and 25% H_2O at room temperature for 3−4 min. For EBSD observation, the polished specimens were electrochemically polished in a solution of 80% CH_3OH and 20% H_2SO_4 at 20 V for 10−15 s. OM study was conducted on an optical microscope (Olympus GX71). EBSD study was conducted on a Quanta 200FEG-SEM scanning electron microscope equipped with OIM analysis software under the voltage of 20 kV and step size in the range of 0.6−1.5 μm.

3 Results and discussion

3.1 Stress–strain curves during isothermal compression

Figure 2 illustrates the typical flow stress curves of GH4037 alloy at different deformation temperatures and different strain rates. As shown in Figs. 2(a) and (b), the flow stress increased sharply at the beginning of deformation. Then, the flow stress increased slowly and reached the peak. At last, the flow stress maintained a steady state of a slight decrease until the end of deformation. However, the curves presented some differences in the third stage at the deformation strain rate of 1 s^{-1}. As shown in Fig. 2(c), these curves showed a relatively steady state without the decrease of flow stress at the third stage in the solid temperature range. When deformation temperature was in the semi-solid temperature range, the flow stress reached the peak quickly, then it kept a steady state in the following deformation, and later the flow stress continued to increase up to the end.

In the first deformation stage, the dislocation generation and multiplication were dominant. Some grains with favorable orientation moved along the slip systems, and the dislocations on different slip planes met at the grain boundaries. Because of the dislocation pile-up, the dislocations were difficult to move and the resistance of dislocation increased. As a result, the effect of work hardening (WH) [29] was obvious. Meanwhile, because the stacking fault energy of GH4037 alloy was relatively low, the dynamic recovery (DRV) was weak to balance the

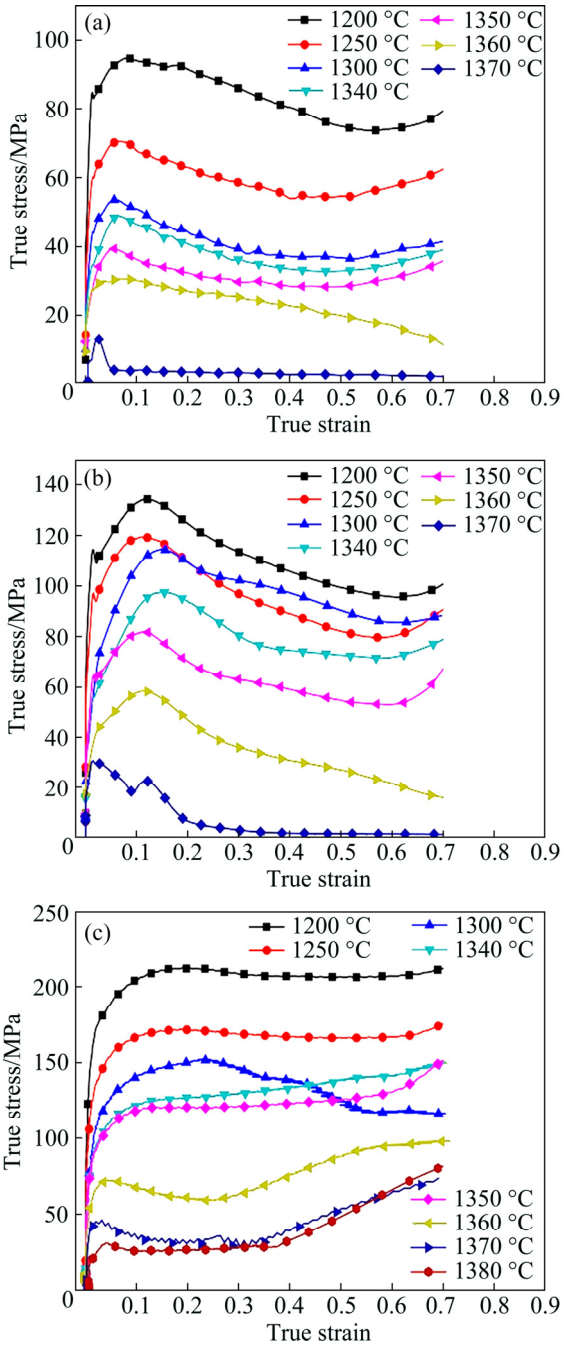

Fig. 2 Flow stress curves of GH4037 at different temperatures and different strain rates: (a) 0.01 s^{-1}; (b) 0.1 s^{-1}; (c) 1 s^{-1}

work hardening [3]. Therefore, the flow stress increased rapidly. In the second stage, when the accumulated dislocation density exceeded a certain value at a critical strain, the dynamic recrystallization (DRX) occurred [30]. The nucleation and growth of recrystallized grains could decrease the dislocation density, which lowered the work hardening rate. Hence, the flow stress increased slowly and reached the peak. In the third stage, the effect of dynamic recrystallization dominated compared to the effect of work hardening. The flow stress kept a steady state with a slight decrease when work hardening and dynamic softening reached a dynamic balance. As for semi-solid deformation, the existence of liquid phase in the compressed samples had a significant influence on compression behaviors. When the strain rates were 0.01 and 0.1 s^{-1}, the liquid phase surrounding the solid matrix had enough time to move to the edge. Because of the small deformation velocity, the compression process was relatively steady. However, when the strain rate was 1 s^{-1}, the whole deformation completed in a very short period of time, the liquid phase hardly had time to move and the softening process would be ended at the same time. The effect of work hardening was highlighted in this process. As a result, the flow stress was still relatively high in the later deformation process.

The strain rate and deformation temperature are the most important influencing factors during hot compression. As shown in Fig. 3(a), the peak stress decreased with the increase of deformation temperature and decrease of strain rate. As shown in Fig. 3(b), the linear relation between $\ln\sigma$ and T^{-1} was fitted in the solid temperature range and semi-solid temperature range, respectively. During hot compression, the cohesive force between atoms decreased with the increase of compression temperature, which resulted in the decrease of critical shear stress and the increase of dislocation movement. Therefore, the flow stress decreased. Because the solid matrix of the specimen was surrounded by liquid phase, deformation temperature had a great influence on flow stress and deformation mechanism. In the solid temperature range, the grains mainly suffered from the plastic deformation; while at semi-solid temperatures, the solid particles could slide or rotate along the liquid phase, which greatly reduced the flow stress [20].

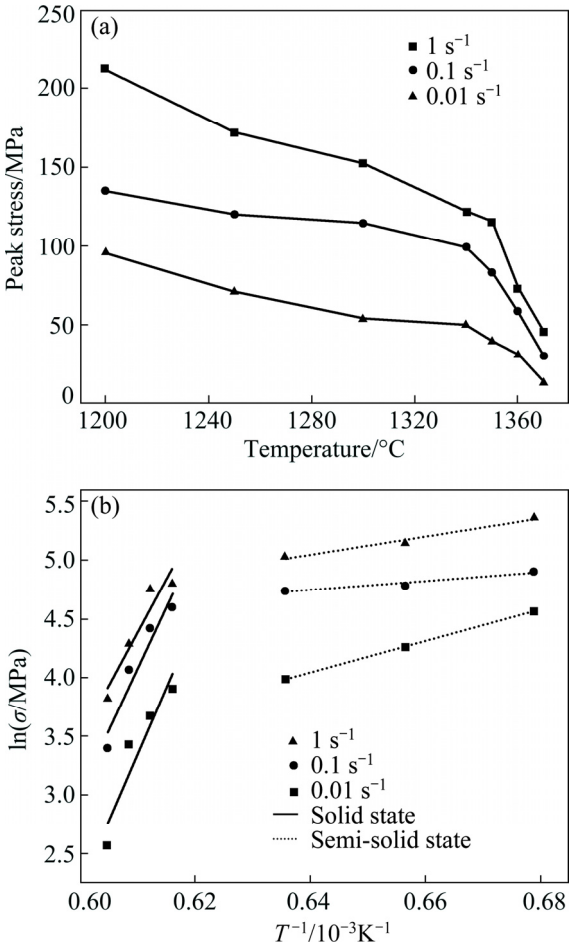

Fig. 3 Effect of temperature on peak stress at different strain rates: (a) Relation of peak stress and compression temperature; (b) Relation of $\ln\sigma$ and T^{-1}

The effect of strain rate on flow stress was also obvious. At low strain rate, the compression velocity was small and the effect of dislocation on the solid grain movement was slight. The deformation resistance was small during compression. High strain rate increased the stored energy and the velocity of dislocation motion, which resulted in the increase of critical shearing strain. Therefore, the work hardening phenomenon was more obvious at higher strain rate in the first deformation stage. At low strain rate, the existence of liquid phase could increase the fluidity of solid grains, which led to the sliding or rotating of solid grains besides elongating. In the meantime, the liquid phase had enough time to move to the edge, which reduced the deformation resistance and made the flow stress in a steady state. At high strain rate, the motion of dislocation and liquid phase was difficult during the short deformation time. Therefore, the deformation resistance was large and

the solid grains were forced to be elongated. At the same time, flow stress did not keep steady in the late deformation at semi-solid compression temperature, which was due to the unbalanced relation between dynamic recrystallization and work hardening.

When the compression temperature was elevated to semi-solid range, the characteristics of viscous fluid occurred in the deformation samples due to the existence of liquid phase. The relationships between apparent viscosity, shear rate and the parameters of hot deformation were investigated, which are given by the following equations [31]:

$$\eta_{\text{app}} = \frac{2\pi h_{\varepsilon}^{4}}{3V^{2}\dot{\varepsilon}} F_{\varepsilon} \tag{1}$$

$$\dot{\gamma}_{\text{av}} = \frac{1}{2}\sqrt{\frac{V}{\pi h_{\varepsilon}^{3}}}\dot{\varepsilon} \tag{2}$$

where η_{app} is the apparent viscosity, $\dot{\gamma}_{\text{av}}$ is the shear rate, h_{ε} is the height of the compressed sample, V is the volume of the sample, F_{ε} is the compression force, and $\dot{\varepsilon}$ is the strain rate. Figure 4 shows the variation of apparent viscosity versus shear rate on a lg−lg plot at semi-solid temperatures. From the fitted lines, the linearity between the logarithm of apparent viscosity and the logarithm of shear rate at different temperatures was good. The apparent viscosity decreased with the increase of deformation temperature and strain rate. The average value of these slopes was −0.78, which indicated a shear thinning behavior of GH4037 alloy in semi-solid state.

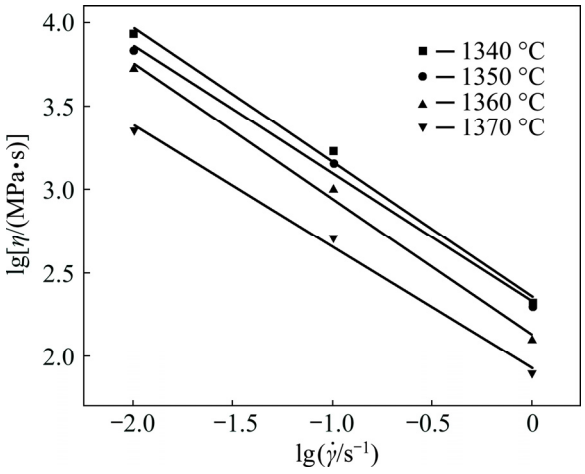

Fig. 4 Variation of apparent viscosity with shear rate at different semi-solid temperatures

3.2 Microstructure evolution of GH4037 alloy during compression

The macrographs of compression samples at different temperatures and different strain rates are shown in Fig. 5. It can be seen that there were no damages and fractures in the round section when the compression occurred at solid temperatures. However, some obvious cracks can be found in the lateral surface of the samples compressed at semi-solid temperatures. With the increase of compression temperature, the fractures were extremely severe. In addition, the lower strain rate led to the appearance of fractures at lower temperature. At 1380 °C, the softening phenomenon was so severe that the compression test could not be carried out at the strain rate of 0.01 s^{-1}.

Fig. 5 Macrographs of compression samples under different deformation conditions

Figure 6 shows the optical microstructures of initial GH4037 alloy before compression. It can be found that the microstructures in the transverse section and longitudinal section of GH4037 alloy bar have little differences. The grains are spherical and there is no orientation difference in these two sections. However, the inhomogeneity of grain size is clear. By the line interception method, the average grain size of initial GH4037 sample is determined to be 23.8 μm.

3.2.1 Microstructures of GH4037 alloy in different deformation zones

During hot compression, the specimens undergo different stress and deformation in different zones. In general, the deformation zones are divided into four parts: hard deformation zone, transition deformation zone, severe deformation zone and free deformation zone [32]. In order to investigate the microstructure evolution of different deformation zones during hot compression, the microstructures of compressed samples in the transverse section and longitudinal section were

observed. Figure 7 shows the microstructures of a quarter specimen compressed at 1250 °C with the strain rate of 1 s^{-1}. The microstructures in different zones corresponded to the diagrammatic sketch in Fig. 7(h). The microstructures observed in Zones a−c were perpendicular to the compression direction, and the microstructures observed in Zones d−g were along the compression direction. In Zones a and d, the microstructures mainly consisted of equiaxed grains. Because of large friction at both ends of the compressed contact surface, the grains in these zones almost suffered from no deformation, namely in hard deformation zone. As shown in Figs. 7(b) and (e), the grains in the transition deformation zone suffered from partial deformation and the grains were elongated obviously. Due to the large deformation degree and high compression temperature, there were a small amount of recrystallized grains around the solid grains. As shown in Figs. 7(c) and (f), a large amount of coarse grains and necklace structures could be found, and many DRX grains dispersed near the grain boundaries. The edge of the compression samples did not suffer from the force directly, so many coarse grains expanded to the free deformation zone. As shown in Zone g, orientation

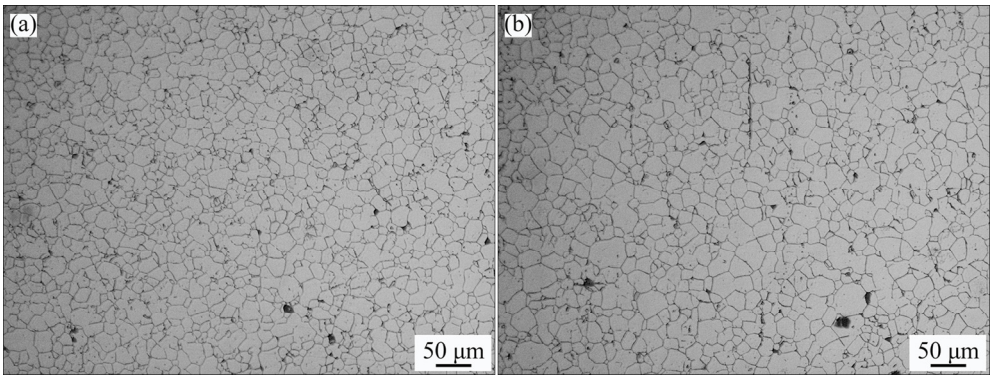

Fig. 6 Microstructures of initial GH4037 alloy before compression: (a) Transverse section; (b) Longitudinal section

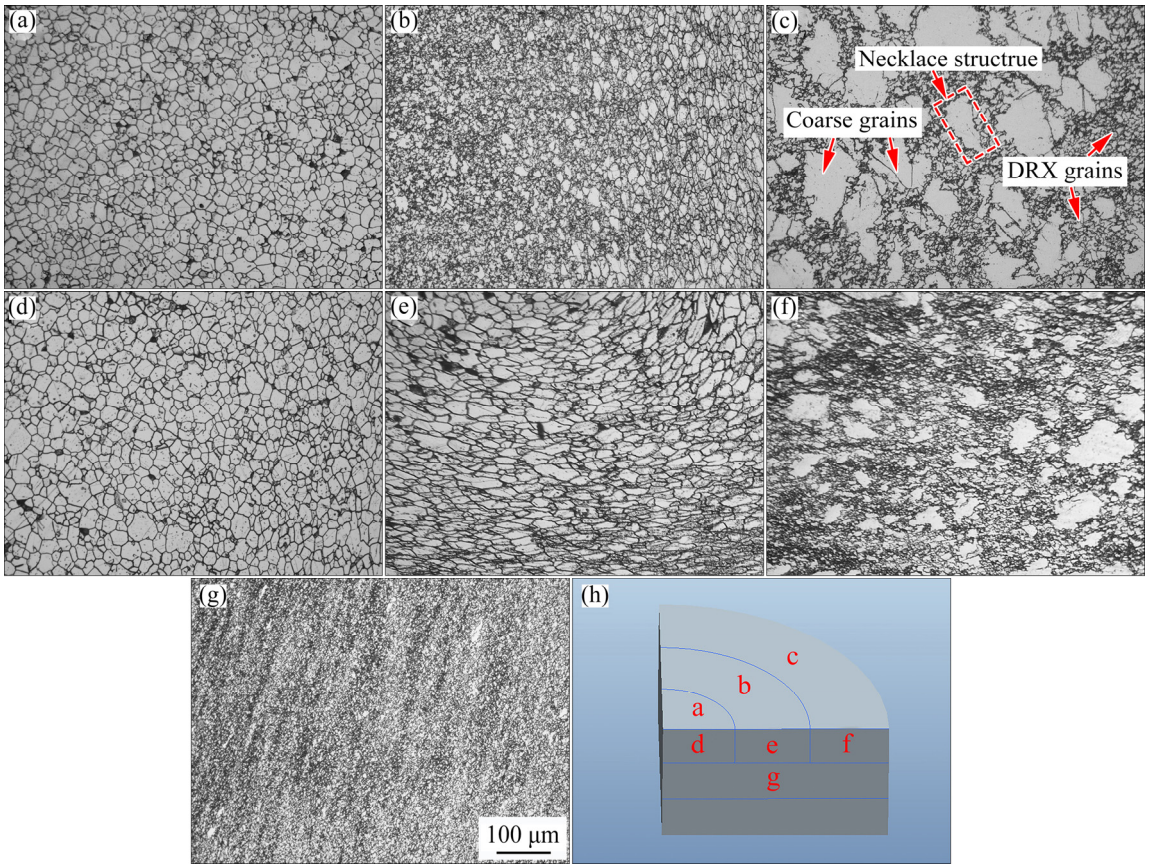

Fig. 7 Microstructures of GH4037 alloy deformed at 1250 °C with strain rate of 1 s^{-1}

of grains was perpendicular to the compression direction. The microstructure in this zone mainly consisted of the fine recrystallized grain. Because of the large strain rate and the short compression time, the recrystallized grains were very small and the grain boundaries were fuzzy in the severe deformation zone.

In order to distinguish the microstructure of GH4037 alloy during hot compression in solid state and semi-solid state, the microstructures of deformed specimens at 1370 °C with a strain rate of 1 s^{-1} were observed. As shown in Fig. 8, the microstructure evolution in different compression zones was approximately similar to that at 1250 °C. Differently, there were partial liquid phases around the solid grains in semi-solid state, and the deformation degree was not so severe in the transition deformation zone compared to that at 1250 °C. However, the flowability was limited because of the large strain rate, which resulted in the same severe deformation in Zone g. Because the compression temperature was high, the growth of the solid grains and DRX grains was obvious.

By comparing the microstructures in solid state and semi-solid state, the deformation mechanism can be recognized. Firstly, the deformation samples underwent different stresses in different zones, which resulted in different microstructures in the center and the edge. In the hard deformation zone, the grains maintained equiaxed morphology because of the large friction at both ends of the compressed contact surface. In the free deformation zone, the grains did not bear stress directly so that the deformation was not obvious. In the severe deformation zone, the grains were elongated and the orientation was vertical to the compression direction. Besides, the dynamic recrystallization occurred during compression. Secondly, the deformation mechanism was different in solid state and semi-solid state. In the solid state, the grains suffered from large plastic deformation. However, in the semi-solid state, the liquid phase surrounded the solid grains. As described in the previous literature [33], semi-solid deformation mechanisms mainly included four major mechanisms: liquid flow (LF), flow of liquid incorporating solid particles (FLS), sliding among solid particles (SS) and plastic deformation of solid particles (PDS). In this work, the solid fraction was relatively high at 1370 °C, so the SS and PDS mechanisms dominated in the deformation process in semi-solid state.

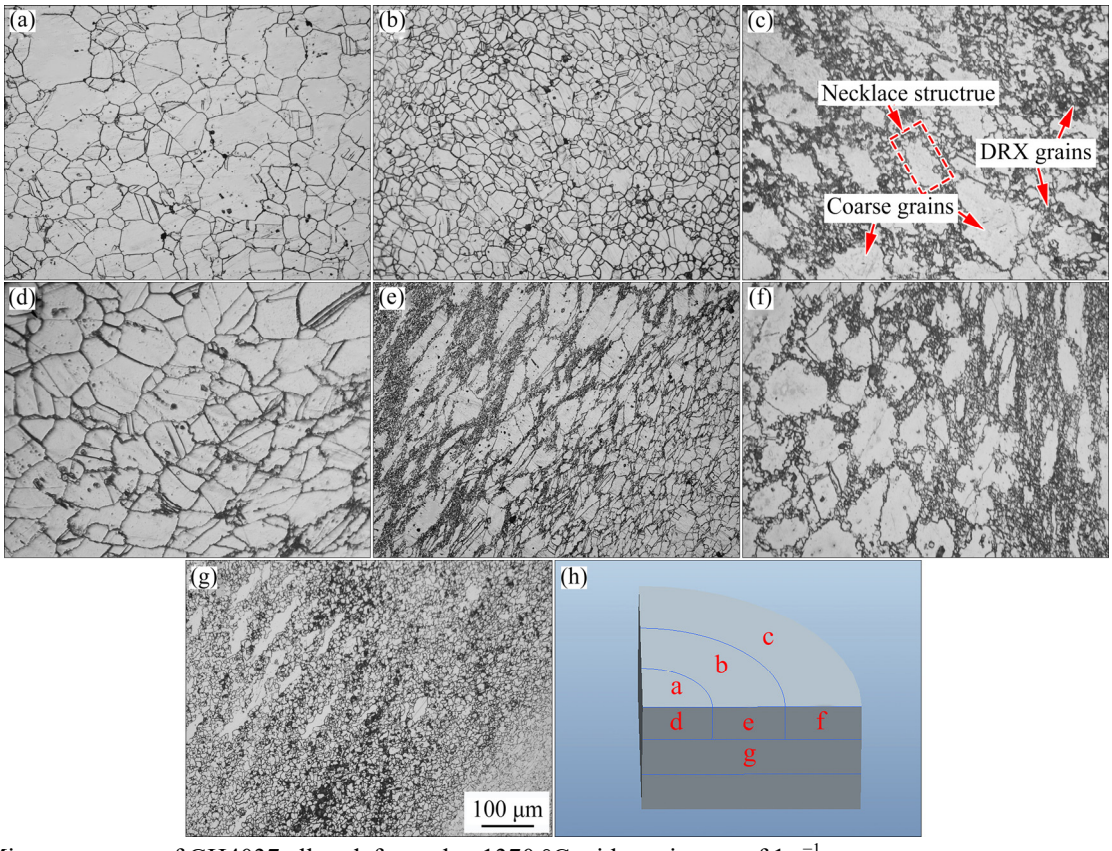

Fig. 8 Microstructures of GH4037 alloy deformed at 1370 °C with strain rate of 1 s^{-1}

3.2.2 Effect of deformation temperature on microstructure evolution

In order to investigate the effect of compression temperature on microstructure, GH4037 specimens were compressed at different temperatures with the strain rate of 1 s^{-1}. Figure 9 shows the microstructures of compressed specimens in solid state (1200 and 1300 °C) and semi-solid state (1360 and 1380 °C) in different zones. It can be found that the grains in Zone a were equiaxed. With the increase of temperature, the grains were more homogenous. In addition, the grain growth was also obvious in Zone a because of the Ostwald ripening mechanism [34]. In Zone b, the initial grains suffered from partial deformation and the solid grains were elongated obviously at 1200 and 1300 °C. When deformation temperature increased to 1360 or 1380 °C, the elongated grains hardly existed and the recrystallized grains were obvious. In Zone c, the necklace structures were obvious and the small DRX grains spread around the large grains. With the increase of temperature, the size of coarse grains and DRX grains at the edge became larger. By comparison, the deformation degree was smaller in semi-solid state than in solid state. In semi-solid state, the liquid phase could improve the flowability of solid grains and decrease the resistance of deformation, so the large solid grains could move to the edge by sliding or rotating without large deformation. In addition, high compression temperature led to the growth of solid grains and DRX grains.

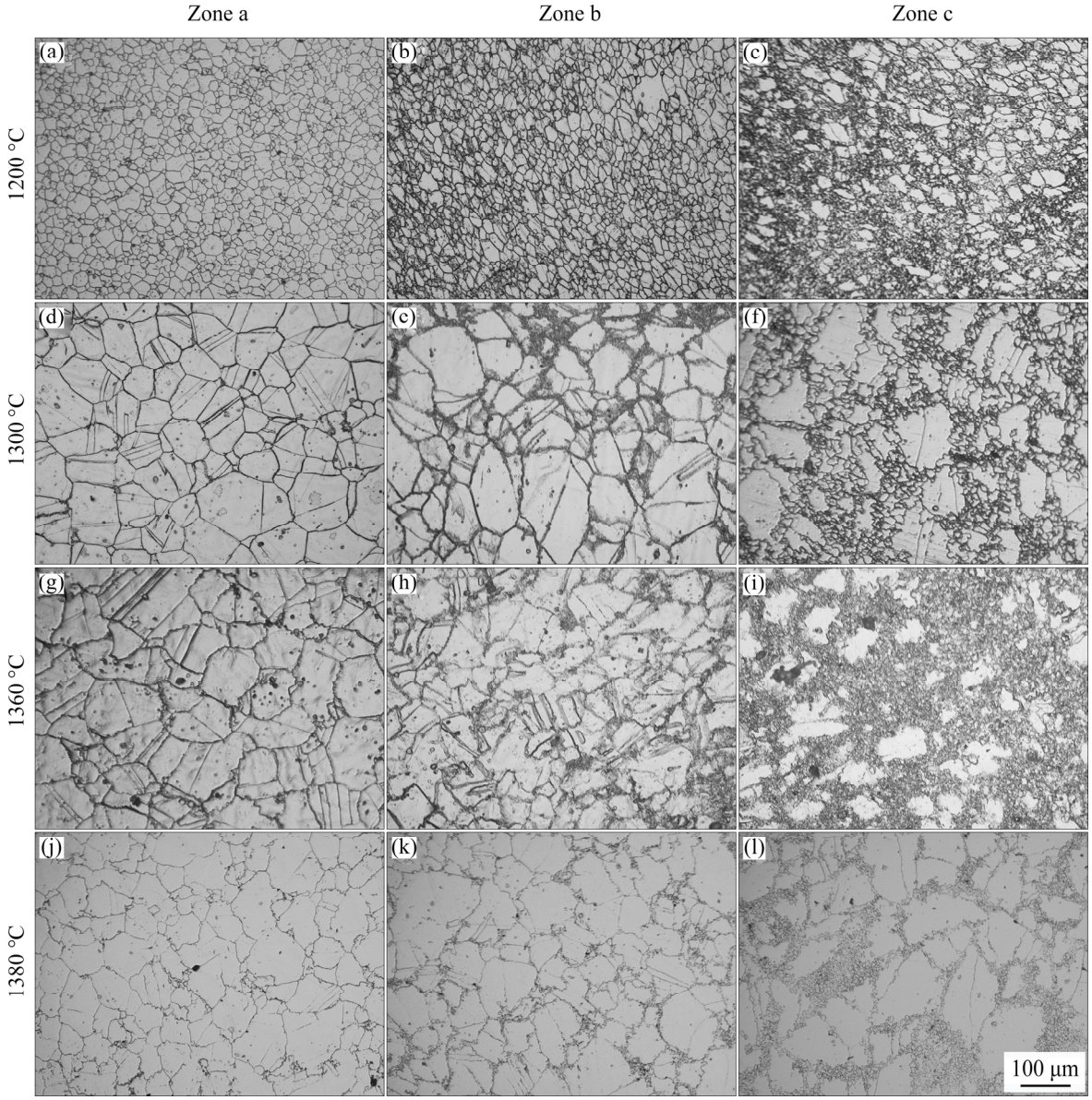

Fig. 9 Microstructures of different zones at strain rate of 1 s^{-1} and different temperatures

3.2.3 Effect of strain rate on microstructure evolution

Figure 10 shows the microstructures of GH4037 specimens in Zone c under different compression conditions. It can be found that when the strain rate was 0.01 s^{-1}, the grains were equiaxed and homogeneous. In addition, as shown in Fig. 10(d), the serrated grain boundaries and small DRX grains could be observed. With the increase of deformation temperature, the grains became larger because of the Ostwald ripening mechanism. As shown in Fig. 10(g), when the temperature was elevated to 1370 °C, the liquid phase appeared in intragranular liquid droplets (LD). At the strain rate of 0.1 s^{-1}, the microstructure evolution was similar to that at the strain rate of 0.01 s^{-1}. In the edge of deformed specimens, the deformation was not severe and the dislocation accumulation was relatively less, so the DRX degree was relatively small. As shown in Fig. 10(j), the grain boundary liquid (GBL) and intragranular liquid droplets (LD) were obvious when the temperature was elevated to 1380 °C. When the strain rate was 1 s^{-1}, the large deformation strain rate contributed to forming a large number of dislocations and structure defects, and large deformation storage energy could increase the nucleation rate, leading to the nucleation of DRX

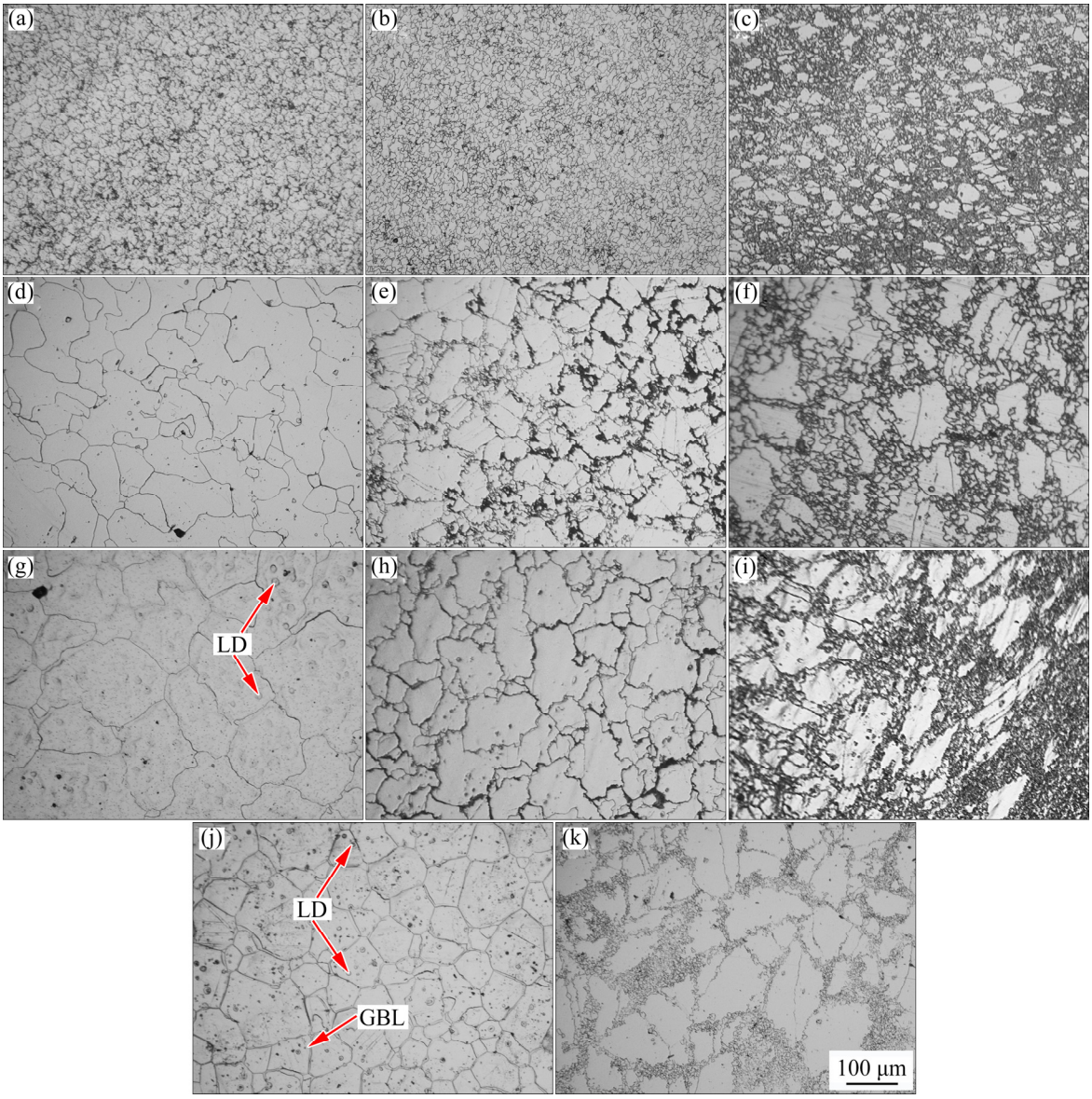

Fig. 10 Microstructures in Zone c of samples compressed at different temperatures and different strain rates: (a) 1200 °C, 0.01 s^{-1}; (b) 1200 °C, 0.1 s^{-1}; (c) 1200 °C, 1 s^{-1}; (d) 1300 °C, 0.01 s^{-1}; (e) 1300 °C, 0.1 s^{-1}; (f) 1300 °C, 1 s^{-1}; (g) 1370 °C, 0.01 s^{-1}; (h) 1370 °C, 0.1 s^{-1}; (i) 1370 °C, 1 s^{-1}; (j) 1380 °C, 0.1 s^{-1}; (k) 1380 °C, 1 s^{-1}

grains. Because of the short deformation time at the strain rate of 1 s^{-1}, the migration of grain boundaries and atoms was limited and the recrystallized grains hardly had time to grow. In conclusion, at low strain rate, the small compression speed decreased the resistance of deformation, and the solid grains and DRX grains had enough time to move and grow. At high strain rate, the deformation was completed in a short time, and the grains suffered from severe deformation and had no time to grow.

3.3 Effect of deformation temperature and strain rate on DRX

In order to investigate the effect of deformation temperature and strain rate on the DRX, EBSD technology was employed. Figure 11 shows the orientation imaging maps and recrystallized fraction maps of GH4037 specimens deformed at 1200 °C. Various colors in the orientation imaging maps demonstrated different orientations. The recrystallized fraction maps indicated the distribution of deformed, substructured and recrystallized grains. Fully recrystallized grains were marked in blue, substructured grains were marked in yellow, and deformed grains were marked in red. As shown in Figs. 11(a) and (b), it can be found that many recrystallized grains were observed and the grains were notably homogeneous at relatively low strain rate of 0.1 s^{-1}. As shown in Figs. 11(c) and (d), the microstructure was mainly composed of elongated deformed grains, and only a few small recrystallized grains nucleated along the deformed grain boundaries. At high strain rate, DRX becomes difficult to occur, and the dynamic recrystallization degree obviously decreased. Apparently, DRX grains appeared in serrated grain boundaries firstly. This was because the high local orientations or strain gradients at serrated grain boundaries were beneficial to the DRX nucleation through grain boundary bulging [35].

Figure 12 shows the orientation imaging maps and recrystallized fraction maps of GH4037 specimens deformed at 1250 °C. It can be observed that the equiaxed and homogeneous grains were obvious. According to the recrystallized fraction maps, it can be found that with the increase of strain rate, the dynamic recrystallization degree and the size of DRX grains decreased.

In order to investigate the DRX evolution of GH4037 specimens deformed at semi-solid temperature, the orientation imaging maps and

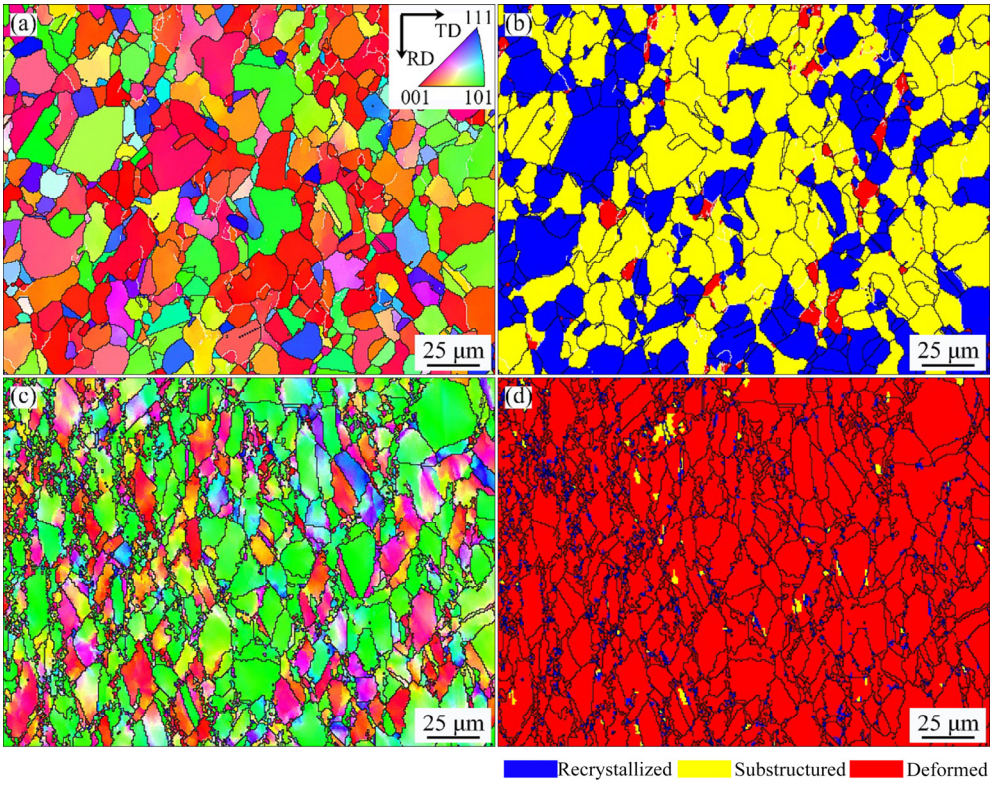

Fig. 11 Orientation imaging maps (a, c) and recrystallized fraction maps (b, d) of GH4037 superalloy deformed at 1200 °C with strain rate of 0.1 s^{-1} (a, b) and 1 s^{-1} (c, d)

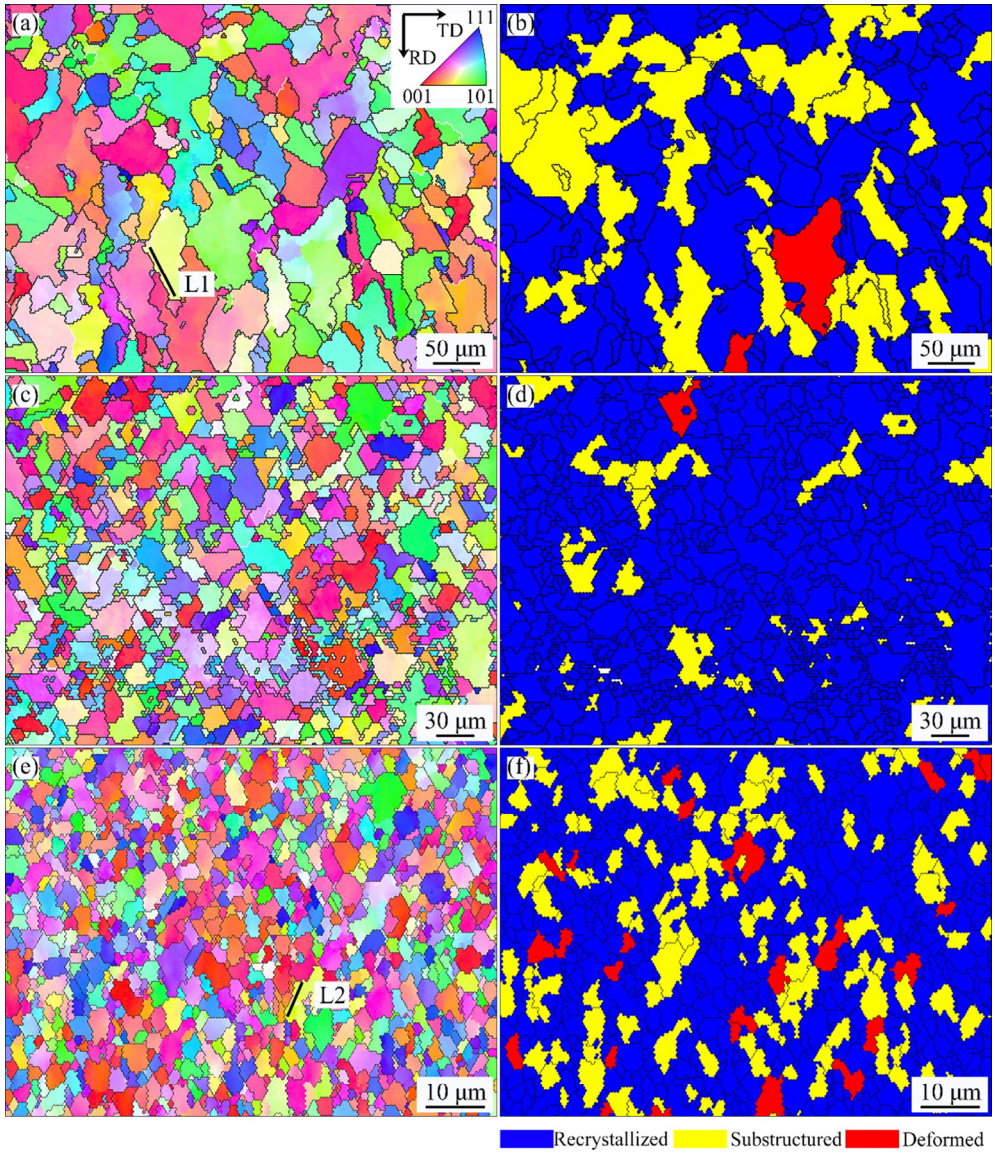

Fig. 12 Orientation imaging maps (a, c, e) and recrystallized fraction maps (b, d, f) of GH4037 alloy deformed at 1250 °C with strain rate of 0.01 s^{-1} (a, b), 0.1 s^{-1} (c, d) and 1 s^{-1} (e, f)

recrystallized fraction maps of GH4037 specimens deformed at 1370 °C are shown in Fig. 13. It can be found that the effect of strain rate on dynamic recrystallization was significant. As shown in Figs. 13(a) and (b), the fraction of recrystallized grains was large and the dynamic recrystallization degree was complete at the strain rate of 0.01 s^{-1}. As shown in Figs. 13(c) and (d), the substructured grains occupied a large percentage at the strain rate of 0.1 s^{-1}. As shown in Figs. 13(e) and (f), there were a large number of deformed grains at the strain rate of 1 s^{-1}.

Generally, the DRX degree increases with the increase of deformation temperature and decrease of strain rate [3,27,36]. Firstly, the deformation temperature has a great effect on dynamic recrystallization of materials. DRX is a thermally-activated procedure, and the nucleation of DRX is mainly caused by the generation, accumulation and interaction of dislocations [3]. The growth of recrystallized grains is caused by the motion of grain boundaries, which is related not only to the stored energy but also to the temperature. With the increase of deformation temperature, the average kinetic energy of atoms increases and the slip resistance of dislocation decreases, which contributes to the nucleation of DRX grains. Meanwhile, high deformation temperature can provide enough driven force for grain boundary migration and thereby accelerates the growth of

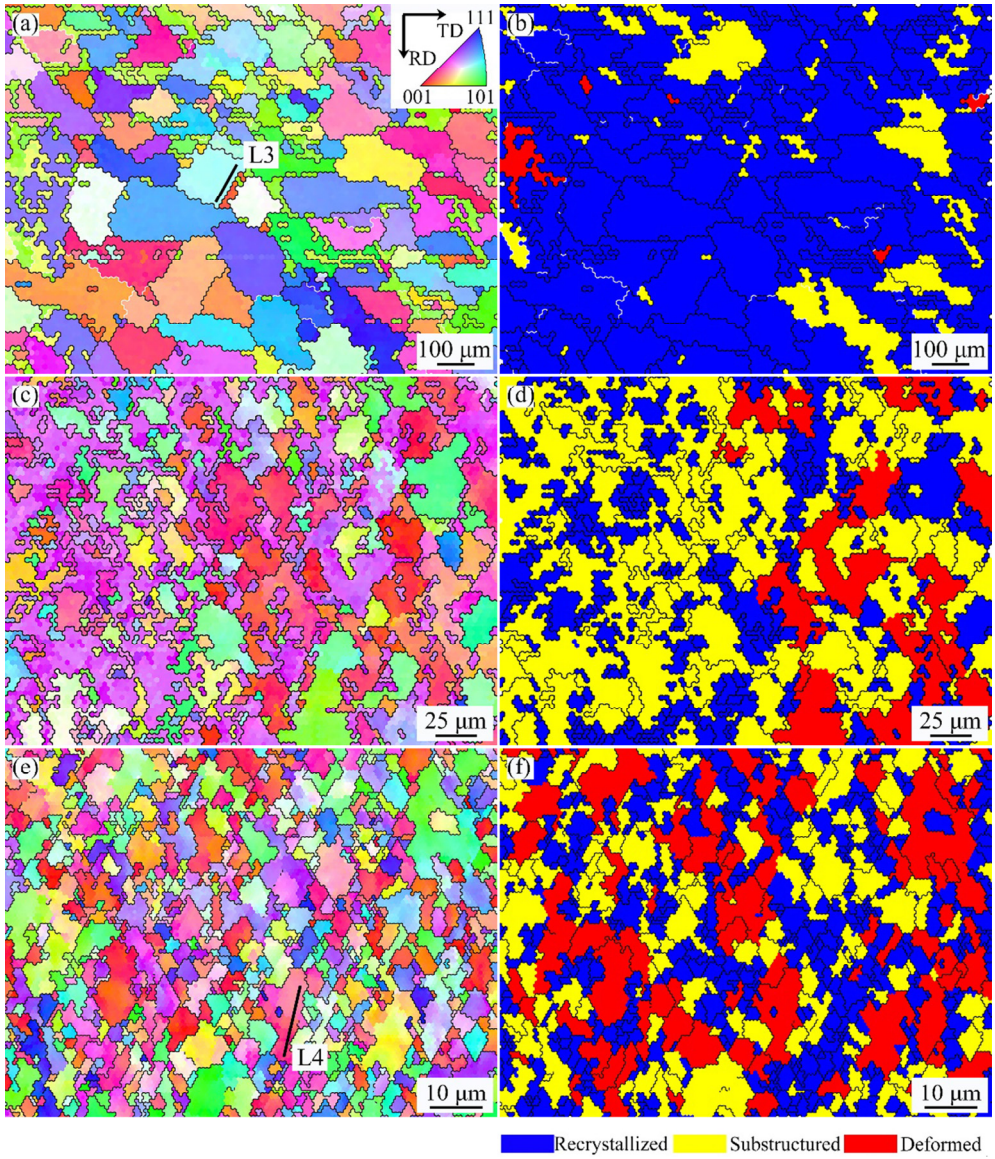

Fig. 13 Orientation imaging maps (a, c, e) and recrystallized fraction maps (b, d, f) of GH4037 alloy deformed at 1370 °C with strain rate of 0.01 s^{-1} (a, b), 0.1 s^{-1} (c, d) and 1 s^{-1} (e, f)

DRX grains. Therefore, the DRX degree is larger at higher deformation temperatures. However, at semi-solid temperatures, the existence of liquid phase has an effect on deformation mechanisms. The sliding between solid particles (SS) and plastic deformation of solid particles (PDS) dominate in the deformation process in semi-solid state. Because of the existence of liquid phase, the solid particles can slid and rotate easily during compression, leading to the decrease of dislocation density. Therefore, the nucleation of DRX grains is inhibited at semi-solid temperatures. Strain rate is another important factor influencing the dynamic recrystallization of materials. At high strain rate, the deformation can provide high dislocation density for the nucleation of DRX grains. However, the limited deformation time restrains the growth of DRX grains. Therefore, dynamic recrystallization degree is relatively low. At low strain rate, the dislocation on the subgrain boundaries has sufficient time to climb and slide, leading to the growth and coalescence of subgrains with small misorientation. Meanwhile, DRX nuclei can form continuously during compression and have enough time to grow. Hence, the dynamic recrystallization degree increases at lower strain rate.

3.4 Misorientation angle evolution

Figure 14 shows the misorientation angle distributions at different strain rates at 1250 °C and

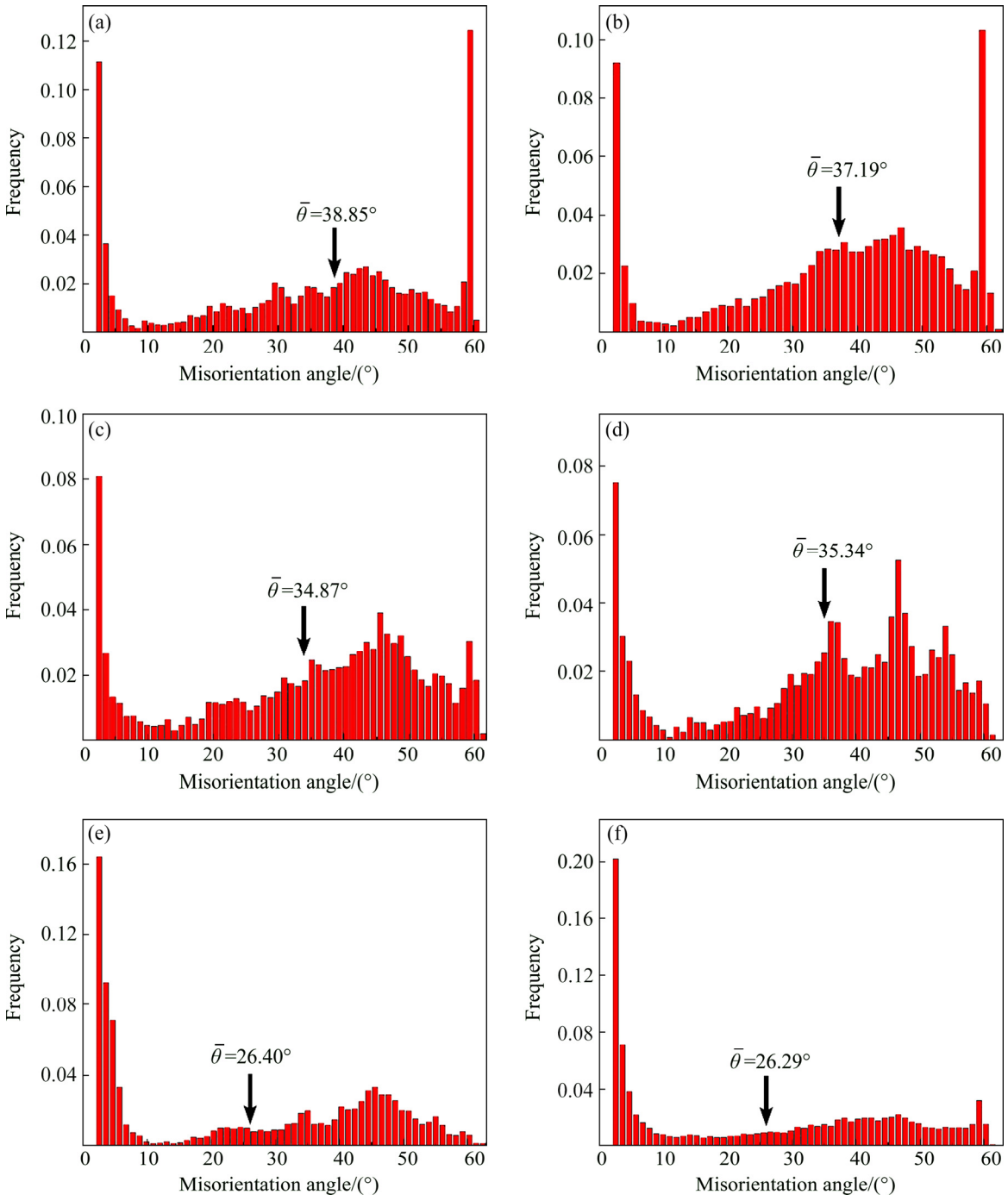

Fig. 14 Misorientation angle distributions of GH4037 specimens compressed at 1250 °C (a, b, c) and 1370 °C (d, e, f) with strain rate of 0.01 s^{-1} (a, d), 0.1 s^{-1} (b, e) and 1 s^{-1} (c, f)

1370 °C. The average misorientation angles of sample compressed at 1250 °C with the strain rates of 0.01, 0.1 and 1 s^{-1} are 38.85°, 37.19° and 34.87°, respectively. The average misorientation angles of sample compressed at 1370 °C with the strain rates of 0.01, 0.1 and 1 s^{-1} are 35.34°, 26.40° and 26.29°, respectively. The increase of average misorientation angle is related to the growth process of DRX nuclei [3]. It can be found that the fraction of high misorientation angles and the average misorientation angles decrease with the increase of strain rate, because high strain rate restrains the growth of DRX grains. In addition to the effect of strain rate on misorientation angle, deformation temperature also has a great influence on misorientation angle. Generally, the average

misorientation angle increases with the increase of deformation temperature, indicating the higher dynamic recrystallization degree at higher deformation temperature. However, the effect of deformation temperature on average misorientation angle is different. As mentioned above, the dislocation density is relatively small at semi-solid deformation temperature because of the sliding between solid particles (SS). Therefore, the nucleation of DRX grains is restrained at semi-solid temperatures, leading to the smaller average misorientation angle. In addition, as shown in Fig. 14, a large percentage of the misorientation angle around 60° can be observed at 1250 °C. This is related to the formation of annealing twins during hot deformation, which can lower the boundary energy of growing grain and increase the mobility of grain boundary [37]. In Fig. 14, the percentage of the misorientation angle around 60° at 1250 °C is larger than that at 1370 °C, indicating a high complete-recrystallization degree at 1250 °C.

3.5 Nucleation mechanisms of DRX

Generally, the main nucleation mechanisms of dynamic recrystallization (DRX) include the three categories: discontinuous dynamic recrystallization (DDRX), continuous dynamic recrystallization (CDRX), and geometric dynamic recrystallization (GDRX) [3,38]. DDRX is characterized by the nucleation and growth of the DRX grains through a bulging mechanism. CDRX is characterized by the progressive rotation of subgrains, resulting in the transformation of low angle subgrain boundaries to high angle grain boundaries. GDRX is distinguished by split of original grains, usually occurring during the severe plastic deformation. In this study, the GDRX can be ignored because of the relatively low strain.

As shown in Fig. 11, it can be found that many grain boundaries are serrated and the small DRX grains form along the serrated grain boundaries. The serrated grain boundaries obtain high local orientation and large strain gradients, which accelerates the nucleation of DRX grains in these regions. As shown in Figs. 12 and 13, with the decrease of strain rate, the recrystallization degree increases and the growth of DRX grains is obvious. The results indicate that DDRX occurs during hot compression. In order to investigate the effect of subgrain rotation on the DRX nucleation mechanism, the changes in the fractions of misorientation angle were evaluated. As shown in Fig. 15, the distribution of misorientation angle at 1250 and 1370 °C with different strain rates can be observed. The misorientation angle of 10°−15° can characterize the CDRX nucleation by subgrain rotatation [39]. In Fig. 15, the fraction of misorientation angle of 10°−15° is relatively small under these deformation conditions, which indicates the small effect of CDRX on nucleation of deformed GH4037 specimens. As shown in Fig. 16, the point-to-point misorientation and the point-to-origin misorientation along the lines labeled in Fig. 12 and Fig. 13 are calculated. In Figs. 16(a, b, c), it can be found that the point-to-point misorientation and the point-to-origin misorientation along the grain boundaries are within 4°. This indicates that the misorientation gradient is relatively steady. However, as shown in Fig. 16(d), the point-to-point misorientation is beyond 9°, demonstrating the progressive subgrain rotation. It is indicated that the CDRX nucleation

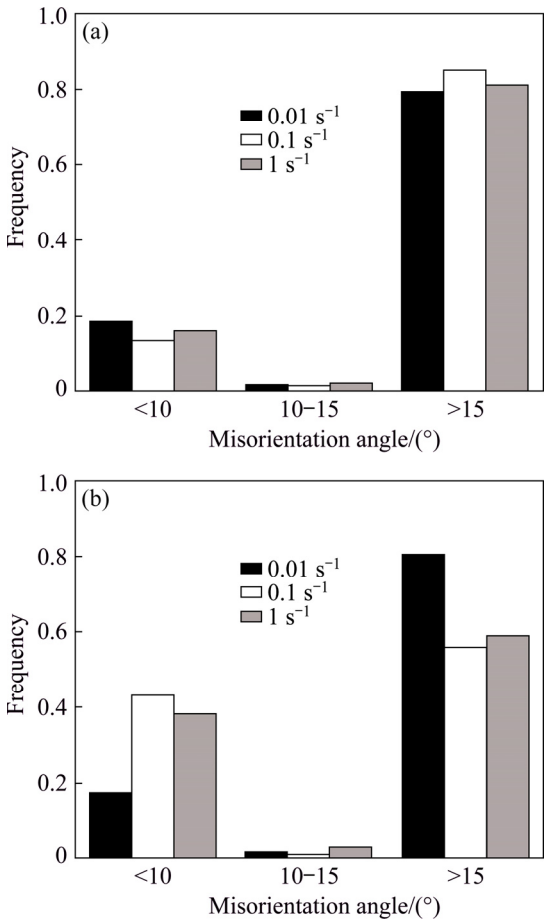

Fig. 15 Changes in fraction of misorientation angle at 1250 °C (a) and 1370 °C (b)

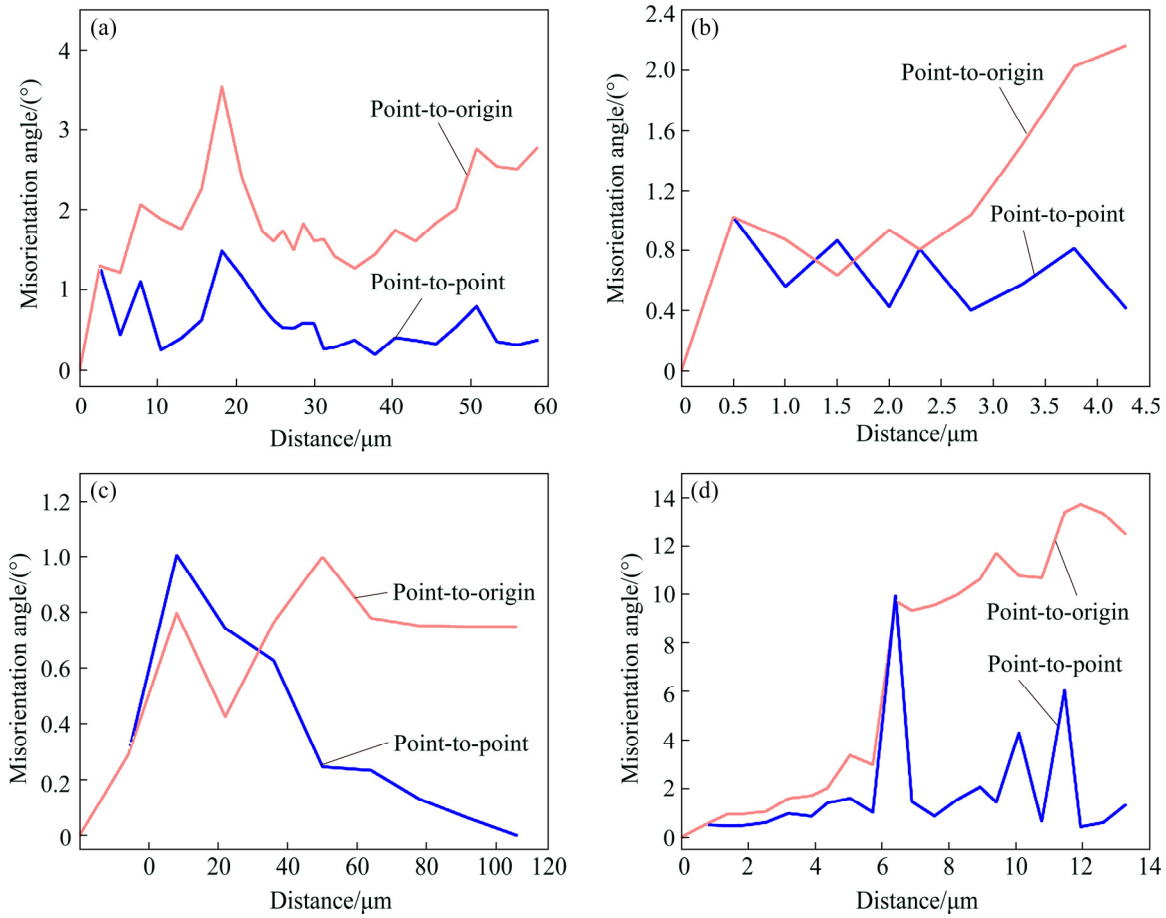

Fig. 16 Changes of misorientation angle along lines labeled in Figs. 12 and 13: (a) L1; (b) L2; (c) L3; (d) L4

mechanism is possible at semi-solid temperatures with high strain rate. Therefore, it can be concluded that the DDRX mechanism is the main nucleation mechanism of GH4037 alloy under these deformation conditions.

4 Conclusions

(1) The flow stress of wrought Ni-based super alloy GH4037 followed the typical stress−strain curve at solid temperatures. Differently, when the strain rate was 1 s^{-1}, the flow stress continued to increase after reaching the initial peak stress at semi-solid temperatures. Besides, the peak stress changed suddenly between solid temperature range and semi-solid temperature range.

(2) The hot deformation zones were divided into four parts. At semi-solid deformation temperatures, the solid grains of deformed specimens were equiaxed and homogeneous, and the liquid phase existed at the grain boundaries and inside the grains.

(3) With the increase of deformation temperature and decrease of strain rate, the dynamic recrystallization degree and the size of DRX grains increased. However, the dynamic recrystallization degree was lower at semi-solid temperatures than at solid temperatures. Discontinuous dynamic recrystallization (DDRX) was the main nucleation mechanism for GH4037 alloy during compression.

(4) In order to obtain homogeneous grains, semi-solid deformation at 1370 and 1380 °C with the strain rate of 0.1 s^{-1} is suggested.

References

[1] LIN Y C, CHEN Xiao-min. A critical review of experimental results and constitutive descriptions for metals and alloys in hot working [J]. Material and Design, 2011, 32: 1733−1759.

[2] SHI Zhao-xia, YAN Xiao-feng, DUAN Chun-hua, ZHAO Ming-han. Effect of strain rate on hot deformation characteristics of GH690 superalloy [J]. Transactions of Nonferrous Metals Society of China, 2017, 27: 538−550.

[3] LIN Y C, WU Xian-yang, CHEN Xiao-min, CHEN Jian, WEN Dong-xu, ZHANG Jin-long, LI Lei-ting. EBSD study of a hot deformed nickel-based superalloy [J]. Journal of Alloys and Compounds, 2015, 640: 101−113.

[4] ZHOU Hai-ping, ZHANG Hong-bin, LIU Jie, QIN Sheng-xue, LV Yu-ting. Prediction of flow stresses for a typical nickel-based superalloy during hot deformation based on dynamic recrystallization kinetic equation [J]. Rare Metal Materials and Engineering, 2018, 47: 3329−3337.

[5] ZHANG Hong-bin, ZHOU Hai-ping, QIN Sheng-xue, LIU Jie, XU Xing-ming. Effect of deformation parameters on twinning evolution during hot deformation in a typical nickel-based superalloy [J]. Materials Science and Engineering A, 2017, 696: 290−298.

[6] ZHOU Yun-kai, FENG Zhi-hao, XIA Chao-qun, LIU Wen-chang, JING Qin, LIANG Shun-xing, MA Ming-zhen, ZHANG Zhi-guo, ZHANG Xin-yu, LIU Ri-ping. Influence of temperature and strain rate on hot deformation behavior of $Zr_{50}Ti_{50}$ alloy in single β field [J], Transactions of Nonferrous Metals Society of China, 2016, 26: 2086−2093.

[7] SPENCER D B, MEHRABIAN R, FLEMINGS M C. Rheological behavior of Sn-15 pct Pb in the crystallization range [J]. Metallurgical and Materials Transactions B, 1972, 3: 1925−1932.

[8] CHO W G, KANG C G. Mechanical properties and their microstructure evaluation in the thixoforming process of semi-solid aluminum alloys [J]. Journal of Materials Processing Technology, 2000, 105: 269−277.

[9] JI S, FAN Z, BEVIS M J. Semi-solid processing of engineering alloys by a twin-screw rheomoulding process [J]. Materials Science and Engineering A, 2001, 299: 210−217.

[10] KLEINER S, BEFFORT O, WAHLEN A, UGGOWITZER P J. Microstructure and mechanical properties of squeeze cast and semi-solid cast Mg−Al alloys [J]. Journal of Light Metals, 2002, 2: 277−280.

[11] FLEMINGS M C. Behavior of metal alloys in the semisolid state [J]. Metallurgical and Transactions B, 1991, 22: 269−293.

[12] LIU Bo, YUAN Xiao-guang, HUANG Hong-jun, ZHANG Shao-hua. Semi-solid deformation of Al−Fe alloy prepared by electromagnetic stirring [J]. Advanced Materials Research, 2011, 152−153: 726−733.

[13] FERRANTE M, FREITAS E R D. Rheological behaviour and deformation characteristics of a commercial and a laboratory-cast Al−4%Cu alloy in the semi-solid state [J]. Acta Materialia, 2001, 49: 3839−3847.

[14] SHANG Shu-zhen, LU Gui-min, TANG Xiao-ling, ZHAO Zu-xin, WU Cheng-ming. Deformation mechanism and forming properties of 6061Al alloys during compression in semi-solid state [J]. Transactions of Nonferrous Metals Society of China, 2010, 20: 1725−1730.

[15] CHINO Y, KOBATA M, IWASAKI H, MABUCHI M. An investigation of compressive deformation behaviour for AZ91 Mg alloy containing a small volume of liquid [J]. Acta Materialia, 2003, 51: 3309−3318.

[16] TANG Qi, ZHOU Ming-yang, FAN Ling-ling, ZHANG Yu-wen, QUAN Gao-feng, LIU Bin. Constitutive behavior of AZ80M magnesium alloy compressed at elevated temperature and containing a small fraction of liquid [J]. Vacuum, 2018, 155: 476−489.

[17] ZHAO Y Q, WU W L, MA X D, CHANG H, YANG H Y, WU H, FENG L. Semi-solid oxidation and deformation behavior of Ti14 alloy [J]. Materials Science and Engineering A, 2004, 373: 315−319.

[18] CHEN Y N, WEI J F, ZHAO Y Q. Compressive deformation and forging behavior of Ti14 alloy in semi-solid state [J]. Materials Science and Engineering A, 2009, 520: 16−22.

[19] REN Fa-cai, CHEN Jun, CHEN Fei. Constitutive modeling of hot deformation behavior of X20Cr13 martensitic stainless steel with strain effect [J]. Transactions of Nonferrous Metals Society of China, 2014, 24: 1407−1413.

[20] MENG Yi, SUGIYAMA S, YANAGIMOTO J. Microstructural evolution during RAP process and deformation behavior of semi-solid SKD61 tool steel [J]. Journal of Materials Processing Technology, 2012, 212: 1731−1741.

[21] LI Jun, YANG Yi-xun, REN Yi-bin, DONG Jia-hui, YANG Ke. Effect of cold deformation on corrosion fatigue behavior of nickel-free high nitrogen austenitic stainless steel for coronary stent application [J]. Journal of Materials Science and Technology, 2018, 34: 660−665.

[22] EZUGWU E O, WANG Z M, MACHADO A R. The machinability of nickel-based alloys: A review [J]. Journal of Materials Processing Technology, 1999, 86: 1−16.

[23] POLLOCK T M, TIN S. Nickel-based superalloys for advanced turbine engines: Chemistry, microstructure and properties [J]. Journal of Propulsion and Power, 2006, 22: 361−374.

[24] PINT B A, DISTEFANO J R, WRIGHT I G. Oxidation resistance: One barrier to moving beyond Ni-base superalloys [J]. Materials Science and Engineering A, 2006, 415: 255−263.

[25] LEWANDOWSKI M S, OVERFELT R A. High temperature deformation behavior of solid and semi-solid alloy 718 [J]. Acta Materialia, 1999, 47: 4695−4710.

[26] CHEN Xiao-min, LIN Y C, WEN Dong-xu, ZHANG Jin-long, HE Min. Dynamic recrystallization behavior of a typical nickel-based superalloy during hot deformation [J]. Material and Design, 2014, 57: 568−577.

[27] WU Yu-ting, LIU Yong-chang, LI Chong, XIA Xing-chuan, HUANG Yuan, LI Hui-jun, WANG Hai-peng. Deformation behavior and processing maps of Ni_3Al-based superalloy during isothermal hot compression [J]. Journal of Alloys and Compounds, 2017, 712: 687−695.

[28] HE Guo-ai, LIU Feng, HUANG Lan, HUANG Zai-wang, JIANG Liang. Microstructure evolutions and nucleation mechanisms of dynamic recrystallization of a powder metallurgy Ni-based superalloy during hot compression [J]. Materials Science and Engineering A, 2016, 677: 496−504.

[29] HUANG J, XU Z. Hot deformation and martensitic transformation behaviors of Fe−32%Ni alloy [J]. Acta Metallurgica Sinica (English letters), 2006, 19: 133−138.

[30] SAMANTARAY D, MANDAL S, JAYALAKSHMI M, ATHREYA C N, BHASURI A K, SARMA V S. New insights into the relationship between dynamic softening phenomena and efficiency of hot working domains of a nitrogen enhanced 316L(N) stainless steel [J]. Materials Science and Engineering A, 2014, 598: 368−375.

[31] GEBELIN J C, SUERY M, FAVIER D. Characterisation of the rheological behaviour in the semi-solid state of grain-refined AZ91 magnesium alloys [J]. Materials Science and Engineering A, 1999, 272: 134−144.

[32] ZHANG Chen-yang, ZHAO Sheng-dun, YAN Guan-hai, WANG Yong-fei. Deformation behaviour and microstructures of semi-solid A356.2 alloy prepared by radial forging process during high solid fraction compression [J]. Proceedings of the Institution of Mechanical Engineers Part B: Journal of Engineering Manufacture, 2016, 232: 487−498.
[33] CHEN C P, TSAO C Y A. Semi-solid deformation of non-dendritic structures−I. Phenomenological behavior [J]. Acta Materialia, 1997, 45: 1955−1968.
[34] ATKINSON H V, LIU D. Microstructural coarsening of semi-solid aluminium alloys [J]. Materials Science and Engineering A, 2008, 496: 439−446.
[35] LIN Y C, HE Dao-guang, CHEN Ming-song, CHEN Xiao-min, ZHAO Chun-yang, MA Xiang, LONG Zhi-li. EBSD analysis of evolution of dynamic recrystallization grains and δ phase in a nickel-based superalloy during hot compressive deformation [J]. Material and Design, 2016, 97: 13−24.
[36] ZHANG Chi, ZHANG Li-wen, SHEN Wen-fei, XU Qian-hong, CUI Yan. The processing map and microstructure evolution of Ni−Cr−Mo-based C276 superalloy during hot compression [J]. Journal of Alloys and Compounds, 2017, 728: 1269−1278.
[37] CORYELL S P, FINDLEY K O, BROWN E. Evolution of microstructure and texture during hot compression of a Ni−Fe−Cr superalloy [J]. Metallurgical and Materials Transactions A, 2012, 43: 633−649.
[38] MEHTONEN S V, KARJALAINEN L P, PORTER D A. Hot deformation behavior and microstructure evolution of a stabilized high-Cr ferritic stainless steel [J]. Materials Science and Engineering A, 2013, 571: 1−12.
[39] LI Kuo-kuo, CHEN Ming-song, LIN Y C, YUAN Wu-quan. Microstructural evolution of an aged Ni-based superalloy under two-stage hot compression with different strain rates [J]. Material and Design, 2016, 111: 344−352.

变形镍基高温合金 GH4037 在固态和半固态下的高温变形行为及组织演变

姜巨福[1]，肖冠菲[1]，王 迎[2]，刘英泽[1]，张 颖[1]

1. 哈尔滨工业大学 材料科学与工程学院，哈尔滨 150001；
2. 哈尔滨工业大学 机电工程学院，哈尔滨 150001

摘 要：镍基高温合金 GH4037 圆柱形试样以不同的应变速率 0.01、0.1 和 1 s^{-1} 在固态温度(1200、1250、1300 °C)和半固态温度(1340、1350、1360、1370、1380 °C)下进行压缩试验，研究 GH4037 合金的高温变形行为及组织演变。结果表明，与固态温度相比，半固体温度下的流动应力下降较快。此外，当应变速率为 1 s^{-1} 时，半固态温度下的流动应力在达到初始峰值应力后继续增大。随着变形温度的升高，初始固相晶粒和再结晶晶粒尺寸增大。在半固态温度下，固相晶粒为等轴晶，液相存在于晶界和晶内。以晶界膨胀为特征的不连续动态再结晶(DDRX)是 GH4037 合金的主要形核机理。

关键词：镍基高温合金；高温变形；半固态；组织演变；动态再结晶

(Edited by Bing YANG)